

# CSST Large Scale Structure Analysis Pipeline: III. Emission-line Redshift Measurement for Slitless Spectra

Jipeng Sui,<sup>1,2</sup> Hu Zou,<sup>1,2\*</sup> Xiaohu Yang,<sup>3,4</sup> Xianzhong Zheng,<sup>5,6</sup> Run Wen,<sup>5,6</sup> Yizhou Gu,<sup>4</sup> Weiyu Ding,<sup>1,6,7</sup> Lu Feng,<sup>1</sup> Hong Guo,<sup>8</sup> Weijian Guo,<sup>1</sup> Yunkun Han,<sup>9</sup> Yipeng Jing,<sup>3,4</sup> Cheng Li,<sup>10</sup> Wenxiong Li,<sup>1</sup> Shufei Liu,<sup>1,2</sup> Zhixia Shen,<sup>1</sup> Gaurav Singh,<sup>1</sup> Jiali Wang,<sup>1</sup> Peng Wei,<sup>11</sup> Yunao Xiao,<sup>1,2</sup> Suijian Xue,<sup>1</sup> Hu Zhan,<sup>12,13</sup> Pengjie Zhang,<sup>3,4</sup> Gongbo Zhao<sup>1,2</sup>

<sup>1</sup>Key Laboratory of Optical Astronomy, National Astronomical Observatories, Chinese Academy of Sciences, Beijing 100101, China

<sup>2</sup>School of Astronomy and Space Science, University of Chinese Academy of Sciences, Beijing 101408, China

<sup>3</sup>Department of Astronomy, School of Physics and Astronomy, Shanghai Jiao Tong University, Shanghai 200240, China

<sup>4</sup>Tsing-Dao Lee Institute, and Key Laboratory for Particle Physics, Astrophysics and Cosmology, Ministry of Education, Shanghai Jiao Tong University, Shanghai 201210, China

<sup>5</sup>Purple Mountain Observatory, Chinese Academy of Sciences, 10 Yuanhua Road, Nanjing 210023, China

<sup>6</sup>School of Astronomy and Space Science, University of Science and Technology of China, Hefei 230026, China

<sup>7</sup>Deep Space Exploration Laboratory / Department of Astronomy, University of Science and Technology of China, Hefei 230026, China

<sup>8</sup>Key Laboratory for Research in Galaxies and Cosmology, Shanghai Astronomical Observatory; Nandan Road 80, Shanghai 200030, China

<sup>9</sup>Yunnan Observatories, Chinese Academy of Sciences, 396 Yangfangwang, Guandu District, Kunming 650216, China

<sup>10</sup>Department of Astronomy, Tsinghua University, Beijing 100084, China

<sup>11</sup>Xinjiang Astronomical Observatory, Chinese Academy of Sciences, Urumqi, Xinjiang 830011, China

<sup>12</sup>National Astronomical Observatories, Chinese Academy of Sciences, Beijing 100101, China

<sup>13</sup>Kavli Institute for Astronomy and Astrophysics, Peking University, Beijing 100871, China

Accepted XXX. Received YYY; in original form ZZZ

## ABSTRACT

The China Space Station Telescope (CSST) is a forthcoming space-based optical telescope designed to co-orbit with the Chinese Space Station. With a planned slitless spectroscopic survey spanning a broad wavelength range of 255 – 1000 nm and a spectral resolution exceeding 200, the CSST holds significant potential for cosmic large-scale structure analysis. In this study, we focus on redshift determinations from slitless spectra through emission line analysis within the CSST framework. Our tailored redshift measurement process involves identifying emission lines in one-dimensional slitless spectra, aligning observed wavelengths with their rest-frame counterparts from prominent galaxy emissions, and calculating wavelength shifts to determine redshifts accurately. To validate our redshift measurement algorithm, we leverage simulated spectra generated by the CSST emulator for slitless spectroscopy. The outcomes demonstrate a remarkable redshift completeness exceeding 85 per cent for emission line galaxies (ELGs), alongside a purity surpassing 83 per cent. The redshift uncertainty remains impressively below 0.001. Notably, when concentrating on galaxies with more than three matched emission lines, both the completeness of ELGs and the purity of measurable galaxies can reach 97 per cent. Furthermore, we explore the influence of parameters like magnitude, spectral signal-to-noise ratio, and redshift on redshift completeness and purity. The discussion also delves into redshift degeneracies stemming from emission-line matching confusion. Our developed redshift measurement process will be applied to extensive simulated datasets and forthcoming CSST slitless spectroscopic observations for further cosmological and extragalactic analyses.

**Key words:** Simulation – Emission Line Galaxy – Sky survey – Spectroscopy Redshift

## 1 INTRODUCTION

Contemporary cosmology has entered an era of precise measurements of cosmological parameters (Cervantes-Cota & Smoot 2011; Wallisch 2019). This advancement is predominantly facilitated by sophisticated observational technologies and analytical methodologies, encompassing high-precision measurements of the cosmic microwave background (Penzias & Wilson 1965; Planck Collabora-

tion et al. 2020), the exploitation of Type Ia supernovae distance-luminosity relationships (Riess et al. 1998), and the investigation of dark matter (Trimble 1987) and dark energy (Peebles & Ratra 2003) properties through phenomena such as baryon acoustic oscillations (Peebles & Yu 1970), redshift-space distortions (Kaiser 1987; Woodfinen et al. 2023), and weak gravitational lensing (Bartelmann & Schneider 2001).

The progress in understanding the evolution of our universe is fundamentally tied to vast quantities of astronomical observational data, with large-scale imaging and spectroscopic surveys serving as

\* E-mail: zouhu@nao.cas.cn

paramount tools. Over the past decades, there are many of such sky surveys providing a vast number of galaxy redshifts, such as the Two-degree Field Galaxy Redshift Survey (2dFGRS) (Colless et al. 2001), the Sloan Digital Sky Survey (SDSS) (York et al. 2000), the Hyper Suprime-Cam Subaru Strategic Program (HSC-SSP) (Aihara et al. 2018), the Dark Energy Survey (DES) (Dark Energy Survey Collaboration et al. 2016), and the Javalambre-Physics of the Accelerated Universe Astrophysical Survey (J-PAS) (Benítez et al. 2014). They have advanced our understanding of the expanding universe and the nature of dark energy.

Presently, a suite of cosmological surveys has been initiated as the Stage-IV dark energy experiments (Albrecht et al. 2006), aiming to explore the expansion history and structure growth of the universe. Among these are prominent ground- and space-based surveys, including Prime Focus Spectrograph (PFS; Tamura et al. 2016), Dark Energy Spectroscopic Instrument (DESI; DESI Collaboration et al. 2016; Lan et al. 2023), Large Synoptic Survey Telescope (LSST; LSST Science Collaboration et al. 2009), China Space Station Telescope (CSST; Zhan 2011, 2021), Euclid (Laureijs et al. 2011), and Roman Space Telescope (RST; Green et al. 2012). These projects signify the dawn of a new era in cosmology, characterised by unprecedented precision of cosmological parameter measurements.

The Chinese Space Station Optical Survey (CSS-OS), utilizing the CSST, will launch a new large-scale cosmological survey featuring both multi-wavelength imaging and slitless spectroscopy (Cao et al. 2018; Gong et al. 2019; Zhan 2021). This survey will cover a sky area of approximately 17,500 square degrees with seven imaging bands and three slitless spectroscopic bands. The telescope is forecasted to significantly advance our understanding of the accelerated expansion of the universe. Comparative assessments indicate that CSS-OS, relative to contemporary weak gravitational lensing and galaxy clustering surveys, will significantly enhance the constraints of cosmological parameters (Gong et al. 2019).

The CSS-OS is designed to facilitate high-precision determinations of cosmological parameters by employing both photometric and spectroscopic redshift measurements. This study narrows its focus to redshift derivations extracted from the CSST slitless spectroscopic data, specifically leveraging the diagnostic power of emission lines. The spectroscopic redshift as well as emission line information of galaxies is also essential for studying the galaxy formation and evolution. We specially develop the process for the redshift determination and evaluate the redshift measurement quality using simulated slitless spectra. These spectra are generated by the CSST Emulator for Slitless Spectroscopy (CESS, Paper II; Wen et al. 2024) using the reference mock galaxy redshift catalogs tying to the photometric data from the DESI legacy imaging surveys (Paper I; Gu et al. 2024).

In this third paper (Paper III) of the series detailing the CSST large scale structure analysis pipeline, the structure of our paper is organized as follows. Section 2 introduces the characteristics of the CSST and CSS-OS slitless spectroscopy. The simulation of the slitless spectra is also summarised in this section. Section 3 depicts the detailed process of the spectroscopic redshift measurement based on nebular emission lines. In Section 4, we apply our redshift measurement method to the simulated CSST slitless spectra to calculate redshifts and assess the redshift quality. The redshift degeneracy due to the emission-line matching confusion and success rate of all redshift outputs are discussed in Section 5. Section 6 gives the summary.

**Table 1.** Key parameters of CSST and related slitless spectroscopy

Parameter	Value
Primary Mirror	2 m
Focal Length	28 m
Imaging quality	PSF $R_{EE80} \leq 0''.15$
Field of View	$\geq 1.1 \text{ deg}^2$ .
Wavelength coverage	0.255 – 1.0 $\mu\text{m}$
	GU: 255–400 nm
Spectral Bands	GV: 400–620 nm
	GI: 620–1000 nm
	GU: 241
Spectral Resolution	GV: 263
	GI: 270
Limiting magnitude (mag) ( $5\sigma$ for point source in AB mag)	GU: 23.2 GV: 23.4 GI: 23.2
Sky coverage of CSS-OS	17500 $\text{deg}^2$

## 2 SLITLESS SPECTRA OF CSST MAIN SKY SURVEY

### 2.1 Main CSST parameters

CSST is a space-based telescope planned by the China Manned Space Program as outlined in Zhan (2011, 2021). It is operated independently yet sharing the same orbit with the China Space Station at approximately 400 km above Earth, which is convenient for routine maintenance. The telescope has a primary mirror of 2 m in diameter and a focal length of 28 m. The radius encircling 80 per cent energy of the point spread function (PSF) is less than  $0''.15$ , which is comparable to that of the Hubble Space Telescope (HST). CSST is equipped with five scientific instruments, including a survey camera, a terahertz receiver, a multichannel imager, an integral field spectrograph, and a cool planet imaging coronagraph. Among these, the survey camera stands out as the cornerstone of CSST observational capabilities, handling both imaging and slitless spectroscopic observations. It provides a field of view of about  $1.1 \text{ deg}^2$ . The wavelength coverage spans from 255 to 1000 nm and the spectral resolution is no less than 200. The survey camera is used to conduct the CSS-OS, which utilises 70 per cent of CSST total observation time over a minimum duration of ten years. This ambitious survey aims to map approximately 17,500 square degrees of the sky, focusing on regions with high Galactic and Ecliptic latitudes. The CSST together with the onboard survey camera are distinguished by a suite of remarkable characteristics: high spatial resolution, exclusive capacity for near-ultraviolet spectral observations, wide wavelength coverage, and large number of filters (Zhan 2021; Gong et al. 2019). This powerful combination is poised to significantly advance our understanding of dark energy, facilitate rigorous tests of gravitational theories, and provide robust validations for cosmological models.

The survey camera at the focal plane contains 30 9k×9k CCD detectors, collectively covering an area of about  $1.1^\circ \times 1.2^\circ$  at the centre of the field of view. Eighteen of these detectors are dedicated to multi-band imaging, armed with filters for NUV (four),  $u$  (two),  $g$  (two),  $r$  (two),  $i$  (two),  $z$  (two), and  $y$  (four) bands. The other twelve detectors are assigned to slitless spectroscopic tasks, employing GU (four), GV (four), and GI (four) gratings. To mitigate technical risks and enhance efficiency, every detector is affixed with a permanent filter or grating. The standard exposure time of 150 s achieves  $5\sigma$  limiting magnitudes for point sources of 23.2, 23.4, and 23.2 mag in the GU, GV, and GI bands, respectively. Additionally, there are plans to survey some deep fields of about  $400 \text{ deg}^2$  with 6.7 times longer exposures (1.2 mag deeper). Nonetheless, the present work confines

its scope to the wide survey. Table 1 lists some key parameters of the telescope and slitless spectroscopy.

## 2.2 Simulation of CSST slitless spectra

To evaluate the capacity of the CSST slitless spectroscopic survey for cosmological constraints, we undertake the development of a comprehensive CSST large scale structure analysis pipeline. This pipeline encompasses an entire sequence, including cosmological simulations, spectral emulation, large-scale structure analyses, and cosmological forecasts. Paper I meticulously outlines the methodology behind assembling the reference mock galaxy redshift catalogs from numerical simulations using presupposed cosmological parameters (Gu et al. 2024). Following this, Paper II introduces the CESS emulator (Wen et al. 2024), which is a pivotal tool designed for the synthesis of slitless spectra from these mock catalogs. Below, we encapsulate the CESS simulation process, and yet encourage readers to refer to Gu et al. (2024) and Wen et al. (2024) for details.

The CESS takes a high-resolution galaxy model spectrum as input and produce a 1D slitless spectrum according to the instrument parameters specific to CSST grisms and detectors, such as wavelength range, spatial and spectral resolution, total throughput, and pixel scale. Additionally, the emulator takes into account the galaxy morphology quantified by four parameters, including Sérsic index ( $n$ ), effective radius ( $R_e$ ), position angle (PA), and axis ratio ( $b/a$ ). These morphological parameters can significantly influence the characteristics of the resulting CSST spectrum. Furthermore, the emulator incorporates various forms of noise, including sky background noise, wavelength calibration error, dark current, and read-out noise. For the sky background estimation, the CESS adopts the data from the HST WFC3 Instrument Handbook (Dressel & Marinelli 2023), providing a specific value of sky background magnitude for each input source according to the sky coordinates.

The emulator employs mock galaxy redshift surveys (MGRSs) sourced from the Jutian numerical simulations to generate its input model spectra. These MGRSs utilise the DESI Legacy Survey dataset (Wright et al. 2010; Zou et al. 2017; Dey et al. 2019), assigning  $z$ -band magnitudes and redshift values up to  $z \sim 1.0$  and imposing a magnitude cut of  $m_z < 21$  mag for galaxies. Subsequently, a photometric analysis of the spectral energy distribution (SED) is conducted with BayeSED (Han & Han 2019) using the five-band DESI photometric data ( $g, r, z, W1$ , and  $W2$ ). This process yields a vast library encompassing over  $10^8$  galaxies, each with a best fitted high-resolution SED alongside other pertinent physical properties. Fig. 1 displays two example spectra from the simulated dataset, each comprising three distinct bands. The spectrum depicted in the upper panel exhibits prominent emission lines, whereas the one in the lower panel lacks clear, identifiable emission lines. The significant fluctuations at the two ends of each spectroscopic channel result from the low instrumental response. For the following analyses of this paper, we combine the spectra from the three channels into a spliced spectrum in an error-weighted manner.

For our redshift analysis, a random subset of approximately  $10^6$  spectra is generated by the CESS emulator. Fig. 2 provides an overview of key parameter distributions: redshift,  $z$ -band magnitudes, and median spectral signal-to-noise ratio (SNR) per pixel. The redshift distribution peaks at a median value of 0.45. The  $z$ -band magnitudes range from 17 to 21 mag, with a median value of about 20.23 mag. Concerning the spectral quality, the SNR distribution skews towards lower values with a median SNR of 2, showing the typical noise levels in our spectral dataset.

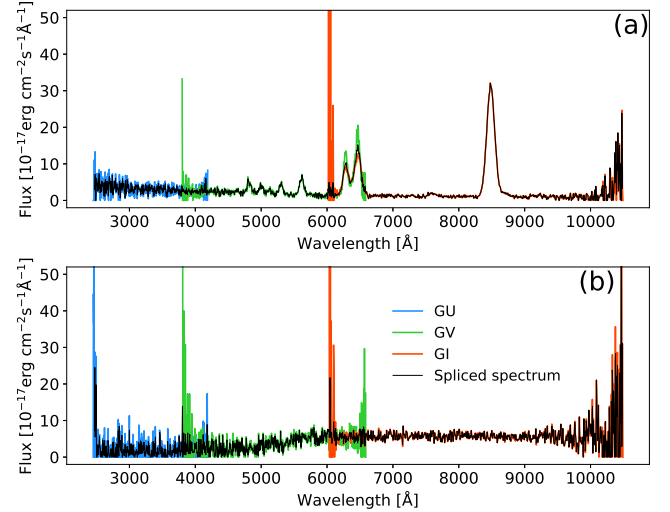


**Figure 1.** Examples of simulated CSST slitless spectra. The solid blue, green, and orange lines represent the GU, GV, and GI spectra, respectively. The black solid lines represent the spliced spectra. The spectrum in the upper panel exhibits clear emission line characteristics, whereas the one in the lower panel does not display prominent emission lines.

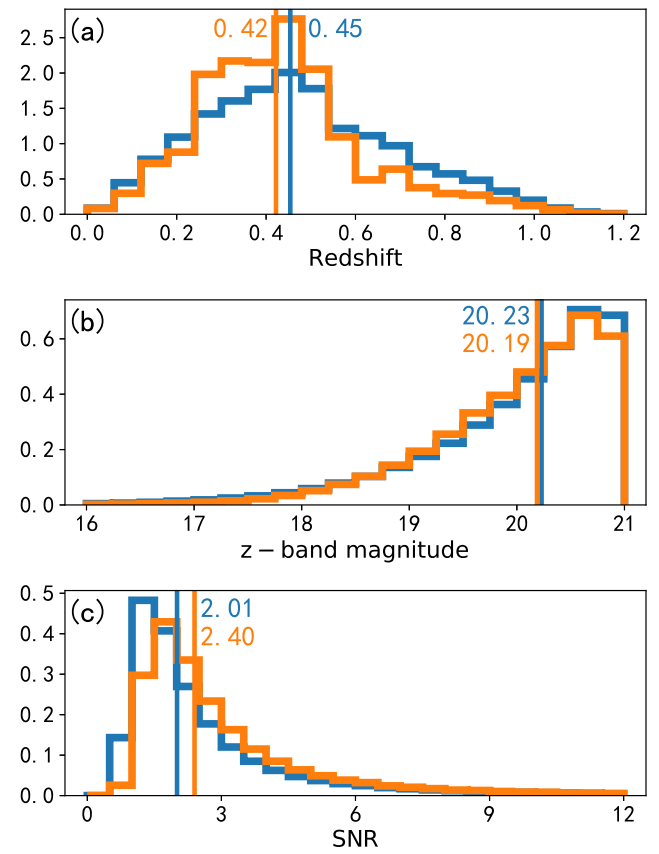


**Figure 2.** Distributions of parameters for all CESS simulated spectra (blue) for redshift (a),  $z$ -band magnitude (b), and SNR per pixel (c). The orange histograms indicate the parameter distributions for spectra with successful redshift measurements (see Section 4.2). Median values are indicated by vertical lines.

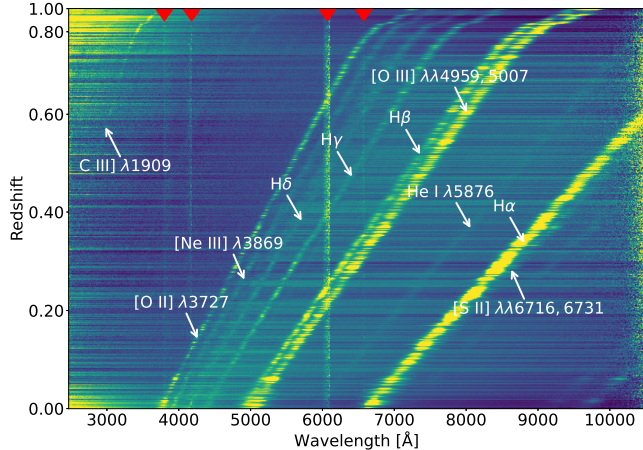


**Figure 3.** Stacked slitless spectra of ELGs, showing the redshifts spanning from 0 to 1, arranged in ascending order from bottom to top. Prominent emission lines are labelled. The flux of each spectrum has been normalised to highlight these emission lines. Notably, the slitless spectra of CSST encompass three separate bands, leading to observable seams between adjacent bands. The presence of low SNRs at the ends of the spectral bands primarily causes these seams. The four red arrows at the top point out the positions of these seams for reference.

### 3 PROCESS OF EMISSION-LINE REDSHIFT MEASUREMENT

#### 3.1 Emission lines

Emission line galaxies (ELGs), characterised by their distinctive spectral emission features originating from ongoing star formation activities, facilitate precise redshift determinations by comparing the observed line wavelengths with their intrinsic counterparts. Fig. 3 showcases the stacked spectra of 1,629 ELGs selected from the CESS simulated data. It illustrates their spectral behavior across a redshift interval of  $0 < z < 1$ . The visualization demonstrates a shift towards longer wavelengths for the most prominent emission lines as redshift increases. Markings within the figure highlight these emission lines, displaying varying intensities in line with established ratios. These characteristic emission patterns serve as crucial elements for precise redshift determinations.

Table 2 lists the key emission lines, serving as templates for redshift determination within the spectral coverage of the CSST slitless grism. The table outlines the detectable redshift ranges and corresponding wavelengths<sup>1</sup> of the template emissions. Notably, for lines such as C IV] $\lambda\lambda$ 1548, 1551, Mg II] $\lambda\lambda$ 2796, 2803, and [S II] $\lambda\lambda$ 6716, 6731, the given wavelengths represent the averages of the two lines. Additionally, the wavelength of [O III]  $\lambda\lambda$ 4959, 5007 is derived as a weighted average based on the flux ratio of 1:2.98 (Brammer 2023). In light of challenges posed by noisy data in the GU band, as highlighted in Fig. 3, certain lines like Ly $\alpha$  and C IV] $\lambda\lambda$ 1548, 1551 may be difficult to distinguish effectively. Furthermore, lines such as [Ne III] $\lambda$ 3869, H $\delta$ , and He I] $\lambda$ 5876 are relatively faint. As a result, this study primarily focuses on prominent lines, including the strong lines [O II]  $\lambda$ 3727, H $\gamma$ , H $\beta$ , [O III]  $\lambda\lambda$ 4959, 5007, H $\alpha$ , and [S II]  $\lambda\lambda$ 6716, 6731. We also include the weaker C III] $\lambda$ 1909, since it is the sole evident ultraviolet emission line as shown in Fig. 3.

**Table 2.** Key emission lines that can be used for redshift determinations

Line name	Wavelength (Å)	Redshift coverage
Ly $\alpha$	1215.670	1.10 – 7.23
C IV] $\lambda\lambda$ 1548, 1551	1549.480	0.65 – 5.45
C III] $\lambda$ 1909	1908.734	0.34 – 4.24
Mg II] $\lambda\lambda$ 2796, 2803	2799.117	0 – 2.57
[O II] $\lambda$ 3727	3727.424	0 – 1.68
[Ne III] $\lambda$ 3869	3868.760	0 – 1.58
H $\delta$	4101.742	0 – 1.44
H $\gamma$	4340.471	0 – 1.30
H $\beta$	4861.333	0 – 1.06
[O III] $\lambda\lambda$ 4959, 5007	4994.800	0 – 1.00
He I] $\lambda$ 5876	5875.624	0 – 0.70
H $\alpha$	6562.819	0 – 0.52
[S II] $\lambda\lambda$ 6716, 6731	6723.625	0 – 0.49

#### 3.2 Basic flowchart

Fig. 4 illustrates the tailored redshift measurement methodology designed for ELGs. It presents the detailed workflow. The sequence encapsulated within the green dashed boundary delineates the core redshift estimation process. The process starts with a 1D slitless spectrum containing wavelengths, fluxes, and corresponding uncertainties. The initial stages involve spectral smoothing and continuum evaluation. Subsequently, peak identification isolates potential emission lines. By comparing these peaks with a reference set of rest-frame emission-line wavelengths, initial redshift solutions are obtained. A minimum of two identifiable emission lines is necessary for the redshift calculation. To refine these estimates, Gaussian fitting is utilised to enhance the accuracy of central wavelength determinations. Ultimately, three top-ranked redshifts are yielded through proper ranking criteria. Each redshift estimation is accompanied by a ZWARNING flag (see Section 3.5) highlighting any potential measurement issues. For validation purposes, the entire process outlined in both the green and black boxes of Fig. 4 is executed. This validation involves calculating SNRs at anticipated emission line wavelengths and assessing redshift quality using the mock galaxy dataset. Here, ELGs are identified based on the presence of at least two emission lines with fluxes surpassing a minimum SNR threshold of 3.

The process for redshift determination is delineated as follows:

(1) *Smoothing and Continuum Estimation:* Commence by obtaining the wavelength, flux, and associated error information from a one-dimensional slitless spectrum. Utilise Gaussian filtering for flux smoothing and estimate the continuum through a combination of median and Gaussian filtering methods.

(2) *Peak Identification:* Adopt a peak detection algorithm (*find\_peaks*<sup>2</sup>) to identify potential emission lines within the smoothed flux spectrum. These lines are identified as those peaks with smoothed fluxes sufficient above the surrounding continuum.

(3) *Emission Line Matching:* Match the identified candidate lines to theoretical emission line templates, and propose potential redshifts. Discard single line matches and remove duplicated matching results.

(4) *Initial Redshift Estimation:* For surviving matches, calculate a preliminary redshift through linear regression of the observed peaks versus template emission line wavelengths.

(5) *Refined Line Analysis:* Enhance precision by applying Gaussian profiles to fit each emission line, extracting more accurate line

<sup>1</sup> <http://astronomy.nmsu.edu/drewski/tableofemissionlines.html>

<sup>2</sup> [https://docs.scipy.org/doc/scipy/reference/generated/scipy.signal.find\\_peaks.html](https://docs.scipy.org/doc/scipy/reference/generated/scipy.signal.find_peaks.html)

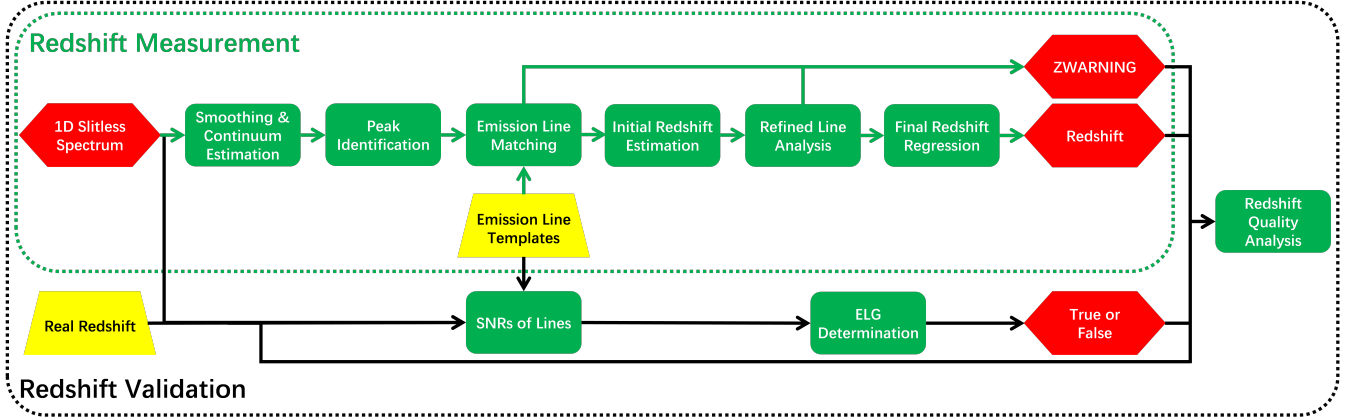


**Figure 4.** Schematic flowchart of the redshift measurement based on emission lines for CSST slitless spectra.

centres and additional parameters (e.g. flux, width, and equivalent width).

(6) *Final Redshift Regression*: Re-evaluate the central wavelengths after Gaussian fitting and undertake another linear regression for refined redshift calculation. During this process, outliers from matched line sets are removed using sigma clipping.

(7) *Redshift Ranking and Output*: Organize all candidate redshifts based on the precision of Gaussian fits and output the top three, if available, alongside their respective errors, number of matched lines, and quality flags of ZWARNING.

The basic inputs include:

- *wave*: Array of wavelengths constituting the input spectrum.
- *flux*: Corresponding flux values in the spectrum.
- *error*: Measurement uncertainty associated with each flux value.
- *rest\_lines*: A list specifying the employed template emission lines for matching, with all feasible options detailed in Table 2.
- *emission\_line\_threshold*: A defined threshold to discriminate significant emission lines during detection.
- *redshift\_upperlimit*: An optional ceiling for considered redshift values; any redshifts surpassing this limit are disregarded.
- *real\_redshift*: The actual redshift of the spectrum, which is for testing purposes only.

Output deliverables include:

- The top three calculated redshifts.
- Associated errors for these redshift estimates.
- ZWARNING flags for these redshift measurements, indicating any potential issues.
- Number of emission lines for determining each of the top three redshifts.
- $\chi^2$  of the redshift fitting.
- Emission line properties, including central wavelengths, fluxes, flux errors, line width, equivalent width, etc.

### 3.3 Emission-line identification and template matching

To detect emission lines in the CSST slitless spectra, we begin by smoothing the spectra and estimating the underlying continua. The smoothing process aims for suppressing the noise while retaining essential spectral features. We achieve this by applying a Gaussian filter using a kernel with the standard deviation of 5 pixels (5 Å per pixel). The smoothed spectra are used for identifying the emission lines. Our approach to estimating the continua involves a two-step

filtering process: a median filter with a window size of 251 pixels and a Gaussian filter with a kernel with the standard deviation of 10 pixels. The latter additional smoothing pass helps to create a more refined estimate of the continuum.

In our analysis, we employ the *find\_peaks* Python module<sup>3</sup> to identify potential emission lines in the smoothed spectrum. This process involves detecting peaks within the spectrum, which are indicative of emission features. To enhance the reliability of our peak detection, we configure several parameters within the *find\_peaks* module. Firstly, a minimum separation of 35 pixels between neighboring peaks is established based on the wavelength distance of template emission lines in the CSST slitless spectra. This separation criterion helps in distinguishing individual peaks and avoiding overlap between nearby fake features. Additionally, we set a minimum width of peaks to 9 pixels. This parameter aids in filtering out noise spikes that do not represent genuine emission features and is specifically tailored to the spectral resolution. Furthermore, the minimal prominence in the *find\_peaks* module is defined as 0.05 times the median flux, which means that the differences between the peak and the baseline height on both sides cannot be less than this value. In addition, the minimal height of peaks is dynamically determined by calculating the sum of the continuum level and a threshold multiplied by the flux error (*continuum + threshold × flux\_error*). This adaptive approach ensures that peaks are detected reliably across varying SNR. Specifically, when the spectral SNR is below 3, the threshold value is set to 0.7. This low threshold is configured to ensure the detection of emission lines with low SNR. As the SNR increases, the threshold value scales logarithmically. By adjusting these parameters based on the spectral characteristics and noise levels, we aim to enhance the precision and robustness of our peak detection methodology for spectra with varying qualities.

After identifying candidate emission lines, the subsequent process involves matching these candidates with template lines to determine their rest-frame wavelengths and associated redshift values. To determine potential redshifts, the identified emission lines are cross-correlated with template emission lines in the following manner: 1) each detected emission line is correlated with each template line to establish a redshift value; 2) a group of at least two emission lines with comparable redshifts is identified within a redshift tolerance of 0.01; 3) a potential redshift is computed using linear regression.

<sup>3</sup> [https://docs.scipy.org/doc/scipy/reference/generated/scipy.signal.find\\_peaks.html](https://docs.scipy.org/doc/scipy/reference/generated/scipy.signal.find_peaks.html)

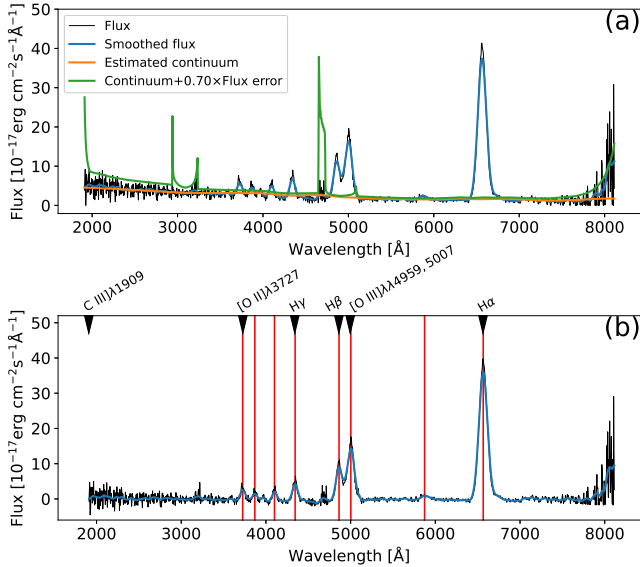


**Figure 5.** A successful redshift measurement. In panel (a), the black curve represents the rest-frame observed spectrum. The blue curve denotes the smoothed spectrum, while the orange curve illustrates the estimated continuum. The green curve indicates the minimum required height for identifying emission lines. Panel (b) displays the emission line identification results. Note that the continuum has been subtracted from the spectrum. The red solid lines highlight the detected candidate emission lines, and black triangles mark the six default template emission lines.

Through this method, all potential redshift values are derived. The example of a successful redshift measurement is illustrated in Fig. 5.

To enhance the precision of central wavelengths, Gaussian fitting is applied to the matched emission lines. When adjacent emission lines are present in a spectrum, multiple Gaussian functions are employed to concurrently fit the profiles of these lines. The background is modelled with a linear function. It is important to emphasize that the final redshift estimation is based solely on the matched template emission lines. This approach is implemented to ensure accuracy in the redshift determination process. The following three cases are handled in this way, including 1) [O II] $\lambda\lambda$ 3727, [Ne III] $\lambda$ 3869, and [Ne III] $\lambda\lambda$ 3967; 2) H $\beta$ , [O III] $\lambda$ 4959, and [O III] $\lambda\lambda$ 5007; 3) H $\alpha$  and [S II] $\lambda\lambda$ 6716, 6731. It should be noticed that [O II] doublet and [S II] doublet are treated as individual lines due to the limited spectral resolution of the CSST slitless spectroscopy. Additionally, the central wavelengths of [O III] $\lambda\lambda$ 4959, 5007 are determined through a weighted average considering their respective fluxes. Fig. 6 showcases the profile fitting process for H $\beta$ , [O III] $\lambda$ 4959, and [O III] $\lambda\lambda$ 5007. All remaining matched emission lines are fitted using a single Gaussian profile.

#### 3.4 Intrinsic line ratios to mitigate the degeneracy

The flux intensities of emission-line galaxies often exhibit strong correlations due to underlying physical conditions of ionization sources (Kewley et al. 2019). Incorrect combinations of emission lines can be effectively eliminated via validating their flux ratios. This verification step plays a crucial role in alleviating degeneracies during the emission line matching process (Brammer 2023), particularly when the number of matched lines is limited. When certain emission lines in a spectrum display flux ratios beyond predefined ranges, the corresponding redshift is flagged with a specific ZWARNING designation

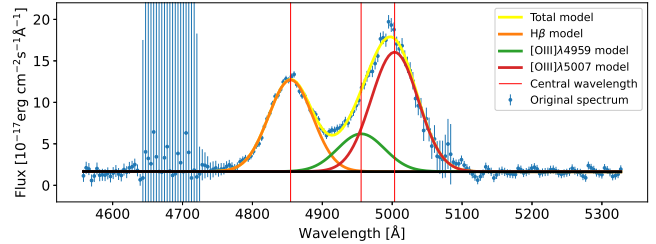


**Figure 6.** Modeling the emission-line profiles within the wavelength range covered by H $\beta$ , [O III] $\lambda$ 4959, and [O III] $\lambda\lambda$ 5007. The blue points with errors represents the fluxes and associated errors. The orange, green, and red curves are the fitted Gaussian profiles for the H $\beta$ , [O III] $\lambda$ 4959, [O III] $\lambda\lambda$ 5007 emission lines, respectively. The black line is the fitted linear background. The yellow curve present the total fitted model. The three red vertical solid lines mark the central wavelengths of the three emission lines.

**Table 3.** Redshift warning flags

Bit	Description
0	The Gaussian profile standard deviation of an emission line reaches the preset maximum value of 100 Å.
1	Observed flux ratio of H $\alpha$ /[S II] < 1.
2	Observed flux ratio of H $\beta$ /[O III] > 2 or < 0.02.
3	Observed flux ratio of [O II]/[Ne III] < 0.3.
4	Observed flux ratio of H $\alpha$ /H $\beta$ < 1.5.
5	Observed flux ratio of [O III]/[O II] < 0.2.
6	Emission lines excluded due to the failure of Gaussian fitting.
7	Observed flux ratio of H $\beta$ /H $\gamma$ < 1.
8	Neither of the two most prominent candidate emission lines could be matched successfully.
9	Observed flux ratio of H $\alpha$ /H $\gamma$ < 2.

(see Section 3.5). To prevent the exclusion of plausible emission line matches, relatively wide ratio ranges are employed. It is worth noting that when the number of matched emission lines is sufficiently large (e.g.,  $\geq 4$ ), the redshift determination is typically accurate without the need for flux ratio constraints. In such cases, the flux ratios do not constrain the redshift estimation process.

#### 3.5 Redshift warning flag

Throughout the redshift measurement process, encountered issues are systematically categorised and documented using the ZWARNING flag. This flag employs a coded system based on powers of 2 ( $2^N$ ), with  $N$  representing a positive integer corresponding to a specific type of issue. These issue types are detailed in Table 3. The magnitude of  $N$  inherently reflects the severity of the encountered problem. The aggregation of  $ZWARNING = \sum 2^N$  consolidates multiple flags into a solitary numeric summary. By interpreting this sum as a binary representation, each bit directly corresponds to a unique issue, where ‘1’ indicates the presence and ‘0’ signifies the absence of the specific problem. Generally, the higher the value of  $N$ , the more frequent the occurrence of redshift measurement failure for this issue.

## 4 QUALITY ANALYSIS OF REDSHIFT MEASUREMENTS

### 4.1 Quality indicators of redshift measurements

The redshift measurement process detailed in Section 3 is subjected to extensive testing to ascertain the accuracy and reliability of its performance using the simulated CSST slitless spectra described in Section 2. Key metrics employed in this evaluation encompass:

- *Bias* ( $\Delta z_{\text{norm}}$ ): measures the systematic offset between the measured and true redshifts. Formulated as  $\Delta z_{\text{norm}} = \frac{z_{\text{Measured}} - \text{Redshift}}{1 + \text{Redshift}}$ , where  $z_{\text{Measured}}$  is the code-derived optimal redshift, and  $\text{Redshift}$  is the input simulation redshift.
- Dispersion ( $\sigma_{\Delta z_{\text{norm}}}$ ): quantifies the scatter in normalized redshift residuals after sigma-clipping to exclude outliers, focusing only on successful measurements ( $|\Delta z_{\text{norm}}| < 0.01$ ).
- *Normalised median absolute deviation* ( $\sigma_{\text{NMAD}}$ ): offers a robust measure of scatter, calculated as  $\sigma_{\text{NMAD}} = 1.48 \times \text{median} |\Delta z_{\text{norm}} - \text{median}(\Delta z_{\text{norm}})|$ , excluding outliers.
- *Outlier rates* ( $P_{0.01}$  and  $P_{3\sigma}$ ): define the fractions of measurements deviating significantly from the true redshift.  $P_{0.01}$  measures the percentage of  $\Delta z_{\text{norm}}$  exceeding 0.01, and  $P_{3\sigma}$  those exceeding  $3\sigma_{\Delta z_{\text{norm}}}$ , relative to the total analysed spectra ( $N_{\text{tot}}$ ).
- *Completeness*: reflects the fraction of measurements achieving specified accuracy, specifically where  $|\Delta z_{\text{norm}}| < 0.01$ , out of all spectra analysed.
- *Purity*: represents the proportion of successful measurements ( $|\Delta z_{\text{norm}}| < 0.01$ ) among all spectra with estimated redshifts.

Unless otherwise specified, references to output redshifts pertain exclusively to the optimal values generated by our redshift measurement method. Furthermore, it is important to emphasize that the configuration yielding the redshift measurement performance in this work has been calibrated specifically for simulated spectra. Consequently, when transitioning to analyse actual observational data from the CSST slitless spectroscopy, a recalibration or tuning of the parameters is imperative to ensure continued accuracy and effectiveness.

### 4.2 Main statistical results of redshift measurements

We have conducted redshift measurements for nearly one million slitless spectra, which were randomly simulated by the CESS as previously described. A synthesis of the quality metrics for these measurements is presented in Table 4. It is worthy to highlight that (1) definition of ELGs: galaxies displaying at least 2 emission lines with SNRs exceeding 3 are categorised as ELGs; (2) successful redshift criteria: a redshift measurement is deemed successful when  $|\Delta z_{\text{norm}}| < 0.01$ ; (3) good redshift quality: redshifts flagged with  $\text{ZWARNING} = 0$  are indicative of high-quality measurements. It is important to emphasize that the redshift determination from a single emission line without additional constraints is impractical for our method of measuring redshift through emission line matching. Our random sample revealed that approximately 21.78 per cent of the galaxies are classified as ELGs. Generally, the purity of redshift measurements reaches 83 per cent, increasing to 91 per cent for measurements tagged with  $\text{ZWARNING} = 0$ . The overall completeness for ELGs stands above 85 per cent, with a 98 per cent purity achieved for ELGs with  $\text{ZWARNING} = 0$ .

In Fig. 2, the orange curve shows the distributions of redshift,  $z$ -band magnitude, and SNR of the spectra with successful redshift measurements. The parameter distributions of these successful cases are roughly the same as those of all spectra shown in blue curves. Compared with the distributions of all spectra, the successfully mea-

**Table 4.** Qualities of redshift measurements based on emission lines for slitless spectra

Item	Value
Number of spectra	1,000,000
Measurable spectra	23.21%
Total successful measurements	19.30%
Purity	83.14%
$\sigma_{\text{NMAD}}$	0.000701
$\sigma_{\Delta z_{\text{norm}}}$	0.000735
$\Delta z_{\text{norm}}$	-0.000128
$P_{3\sigma}$	0.017493
Purity with $\text{ZWARNING} = 0$	91.17%
Number of ELGs	21.78%
Measurable ELGs	90.51%
Completeness of ELGs	85.21%
$\sigma_{\text{NMAD}}$ of ELGs	0.000684
$\sigma_{\Delta z_{\text{norm}}}$ of ELGs	0.000716
$\Delta z_{\text{norm}}$ of ELGs	-0.000129
$P_{3\sigma}$ of ELGs	0.016412
Purity of ELGs with $\text{ZWARNING} = 0$	98.28%

sured ones tend to have slightly lower redshifts, brighter magnitudes, and larger SNRs.

### 4.3 Completeness, purity and accuracy

Fig. 7 provides a comprehensive view of the redshift completeness for ELGs within our simulated slitless spectral dataset. These completenesses are systematically examined in relation to three fundamental parameters, including the SNR, redshift, and  $z$ -band magnitude. To ensure balanced comparisons and statistically meaningful insights, the data has been strategically binned such that each bin encapsulates an approximately equal number of galaxies.

Fig. 7a illustrates the variation in the completeness of redshift measurements for ELGs with respect to the SNR. A gradual ascent in completeness is observed as SNR improves, ranging from approximately 74 per cent to 91 per cent. Notably, the completeness at the maximum SNR bin is marginally lower, primarily due to misidentifications of ELGs induced by fluctuations in the continua. Fig. 7b depicts the completeness as function of redshift. It reveals a modest decline in completeness as redshift increases. Fig. 7c explores how completeness varies with respect to  $z$ -band magnitudes. The data highlights a peak completeness reaching about 89 per cent occurring at  $z \sim 19.1$ . Beyond this magnitude, completeness diminishes. At brighter magnitudes, this reduction can be ascribed to both the relative scarcity of luminous ELGs and the incorrect ELG classification. Conversely, despite the abundance of objects with fainter magnitudes, their inherently lower SNR complicates redshift determinations, thereby contributing to a decline in overall completeness.

The assessment of redshift measurement purity, defined as the fraction of correct redshift determinations among all measurement results, is conducted across varying SNRs, redshifts, and  $z$ -band magnitudes. Fig. 8 depicts the changes in purity corresponding to these parameters. Specifically, Fig. 8a reveals that the purity bottoms out at around 59 per cent for the lowest SNR bin, indicative of a large fraction of unsuccessful measurements. A marked improvement is observed as SNR rises, with purity almost reaching 87 per cent once SNR exceeds 2. Furthermore, Fig. 8b evidences a downturn in purity as redshift increases. Purity remains above 80 per cent at lower redshifts but tails off to approximately 75 per cent beyond redshift 0.6. The overall purity maintains a level greater than 80 per cent across all magnitude ranges.

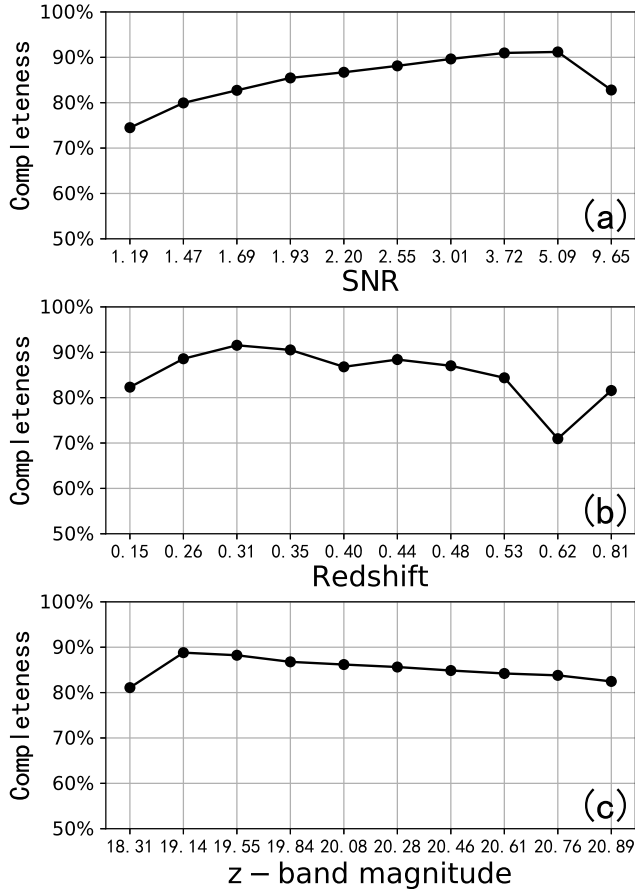


**Figure 7.** Completeness for ELGs as functions of spectral SNR (a), redshift (b), and  $z$ -band magnitude (c).

Fig. 9 depicts the redshift accuracy, quantified by  $\sigma_{\text{NMAD}}$ , for spectra with successful redshift determinations, in relation to SNR, redshift, and  $z$ -band magnitude. Evidently, the accuracy progressively enhances alongside rising SNR, spanning values from over 0.001 at an SNR of 1.10 to a minimum of 0.0005 when SNR exceeds 5. While displaying some fluctuations, the trend shows a general decrease in accuracy with increasing redshift. Additionally, the accuracy decreases with respect to  $z$ -band magnitude, starting at slightly over 0.0005 for magnitudes around 18.4 and climbing to 0.0008 at magnitudes reaching 20.9. A crucial consideration in interpreting these accuracy measures is their notable dependence on the presupposed wavelength calibration error. Specifically, a typical wavelength error of 0.1% was adopted for the simulation in Paper II.

#### 4.4 Effect of the number of matched lines

The quality of redshift measurements should be also related to the number of matched emission lines in the galaxy spectra. These matched emission lines encompass both the genuine emission lines inherent to the galaxy, as well as any erroneously identified lines, hence have impact on the redshift measurements. Fig. 10 shows the performance metrics of completeness, purity, and  $\sigma_{\text{NMAD}}$  in relation to the number of matched emission lines ( $N_{\text{line}}$ ). When four or more lines are matched, the redshift measurements achieve near-perfect scores (close to 100%). With three matched lines, the figures re-

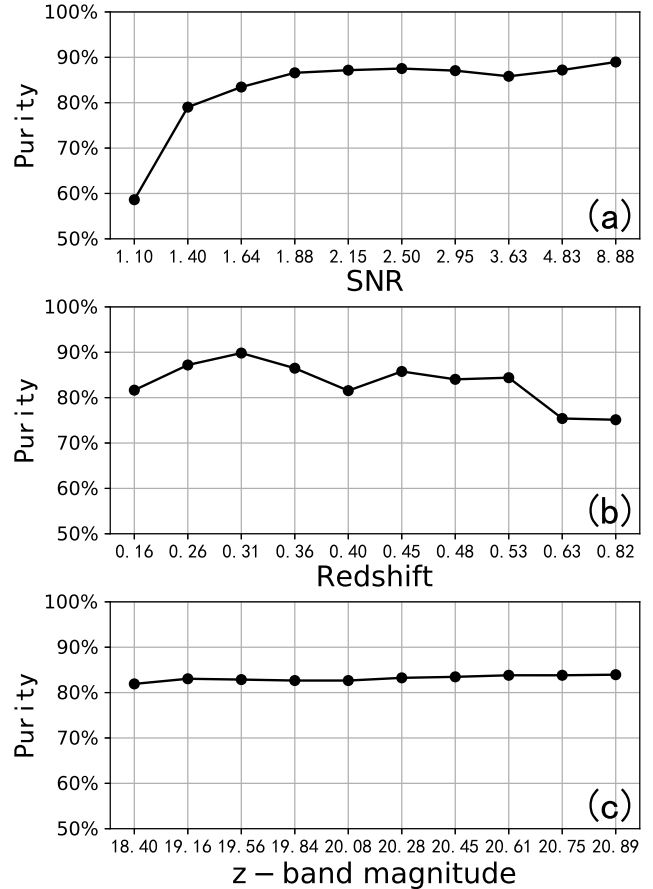


**Figure 8.** Purity for all measurable spectra as functions of spectral SNR (a), redshift (b), and  $z$ -band magnitude (c), respectively.

main high at no less than 96% for both completeness and purity. If  $N_{\text{line}} = 2$ , we can observe that a substantial dip in both completeness and purity to about 86% and 64%, respectively. The lower panel of Fig. 10 discloses a direct inverse association between  $\sigma_{\text{NMAD}}$  and  $N_{\text{line}}$ , illustrating a decline from 0.0010 at  $N_{\text{line}} = 2$  down to 0.0004 when  $N_{\text{line}} \geq 5$ .

#### 4.5 Redshift quality for different sample selections

Fig. 11 presents a comparison between the measured redshifts ( $z_{\text{Measured}}$ ) with the true redshifts for different sample selections. The left columns show the comparison of all measurable spectra and identified ELGs, the middle columns display the samples where the redshift measurements have  $Z\text{WARNING} = 0$ , and the right columns contain the samples with both  $Z\text{WARNING} = 0$  and  $N_{\text{line}} \geq 3$ . Ideally, every measured redshift would perfectly align with its corresponding intrinsic redshift, resulting in an diagonal in each panel. The figure illustrates that points closest to the diagonals exhibit highest densities. The majority of measurable values and ELG values fall within an acceptable tolerance zone, indicating successful measurements. However, some measured redshift values notably deviate from the simulated values, suggesting unsuccessful outcomes. Interestingly, certain unsuccessful measurements cluster together, forming distinct strips. This clustering pattern may indicate systematic confusions in emission line matching, which will be discussed in

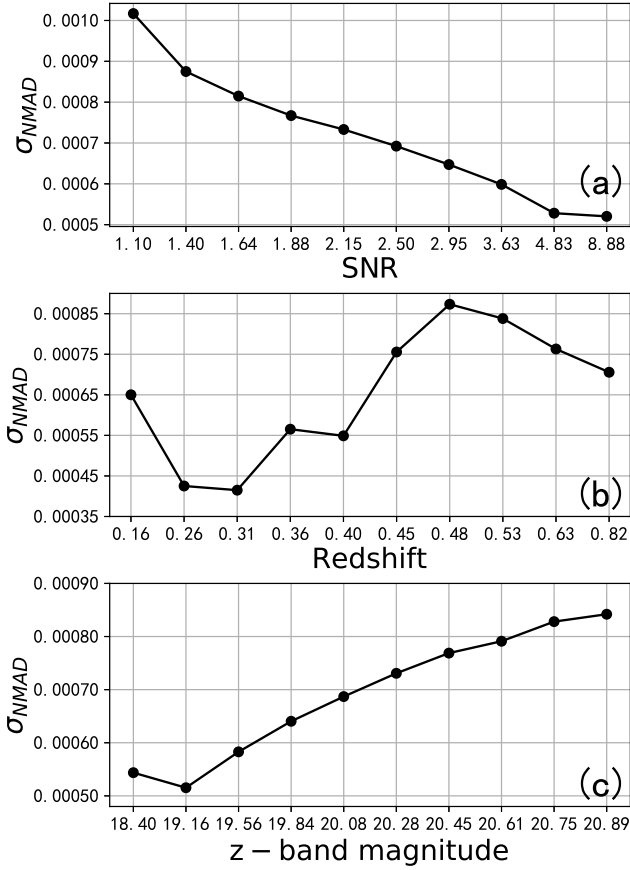


**Figure 9.**  $\sigma_{\text{NMAD}}$ s of all successfully measured spectra as functions of spectral SNR (a), redshift (b), and  $z$ -band magnitude (c), respectively.

Section 5.1. Overall, incorporating the redshift quality flag and the number of matched emission lines can greatly enhance the purity of the results. However, this refinement may also lead to a significant decrease in the completeness.

## 5 DISCUSSION ON REDSHIFT MEASUREMENTS

### 5.1 Redshift degeneracy due to mismatching of emission lines

The erroneous redshift determinations attributed to mismatching of emission lines persist, so we employ the flux ratios of emission lines as a means to constrain our matching procedure. These mismatches can stem from inaccuracies in flux measurement due to the low SNR or the presence of non-typical physical conditions within the source, consequently giving rise to redshift ambiguities. Fig. 12 illustrates the redshift degeneracy for ELGs caused by the wrong matching of emission lines. The labels in this figure aid in discerning the correlation between the measured and simulated redshifts, thereby confirming instances of wrong matched lines. The redshift degeneracy observed above the diagonal within Fig. 12 arises from the misidentification of longer-wavelength emission features as shorter-wavelength ones. Conversely, beneath the diagonal, the issue lies in shorter-wavelength lines being incorrectly interpreted as longer-wavelength ones.

Generally, two primary scenarios can lead to the incorrect matching of emission lines. Firstly, genuine lines may be misinterpreted, particularly in cases where only two detected lines are present. Due to

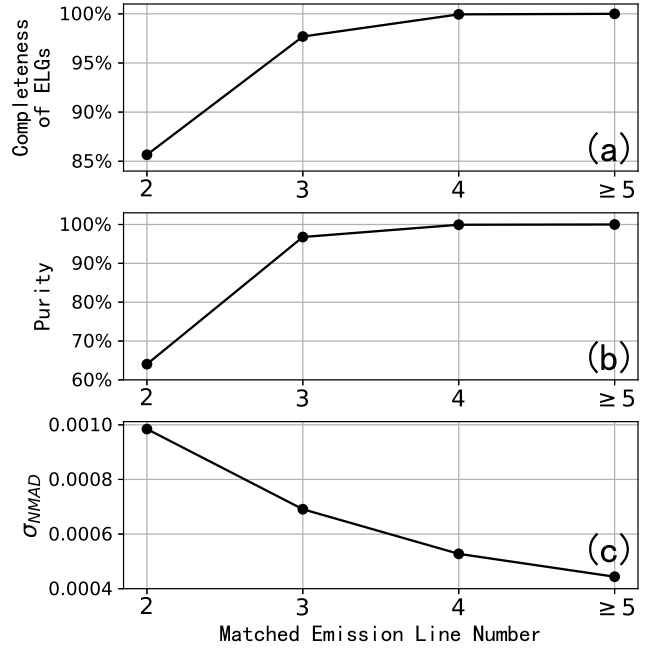


**Figure 10.** The completeness (a), the purity (b) and accuracy  $\sigma_{\text{NMAD}}$  (c) as function of the number of matched emission lines ( $N_{\text{line}}$ ).

measurement uncertainties and low spectral resolution, some cases of confusion may arise from pairs of these lines being mistaken, such as H $\alpha$  and [O III] being confused with H $\beta$  and [O II], H $\alpha$  and H $\beta$  being confused with [O III] and [O II]. Secondly, confusion can occur when detected lines are spurious. A systematic error in redshift determination can occur when one genuine line is erroneously paired with fake lines. For example, [O II] may be confused with C III], H $\alpha$  may be confused with [O II] or H $\gamma$ , H $\beta$  may be confused with H $\gamma$ , and [O III] may be confused with H $\beta$ .

Table 5 provides the fractions of spectra due to different emission-line confusions for both ELGs and all measurable galaxies. The various degeneracy scenarios contribute differently to measurement failures. Typically, there is a higher incidence of situations where longer wavelength emission lines are mistakenly identified as shorter ones, resulting in systematically higher redshift measurements. This trend is primarily attributed to the fact that lower-redshift galaxies tend to exhibit relatively higher SNRs, increasing the chances of incorrect line matching. Applying a cut of ZWARNING = 0, where the flux ratios of emission lines are confined, or requiring a minimum number of matched line can significantly reduce the occurrence of confusion cases (as shown in Fig. 12).

### 5.2 Redshift success rate of top three redshift outputs

Our redshift measurement process allows for a maximum of three redshift estimates. However, confusion arising from matching emission lines can impact the precision of redshift estimation, potentially affecting the accuracy of the primary redshift estimate. As a result, the secondary and tertiary estimates, while ranked lower, may still provide valid alternatives. A "successful redshift cover" is defined when at least one of top three redshift outputs is correct. Correspondingly, the redshift covering rate is calculated as the proportion of successful covers among the total redshift measurements. Table 6 presents the success rates of the three redshift outputs for ELGs and

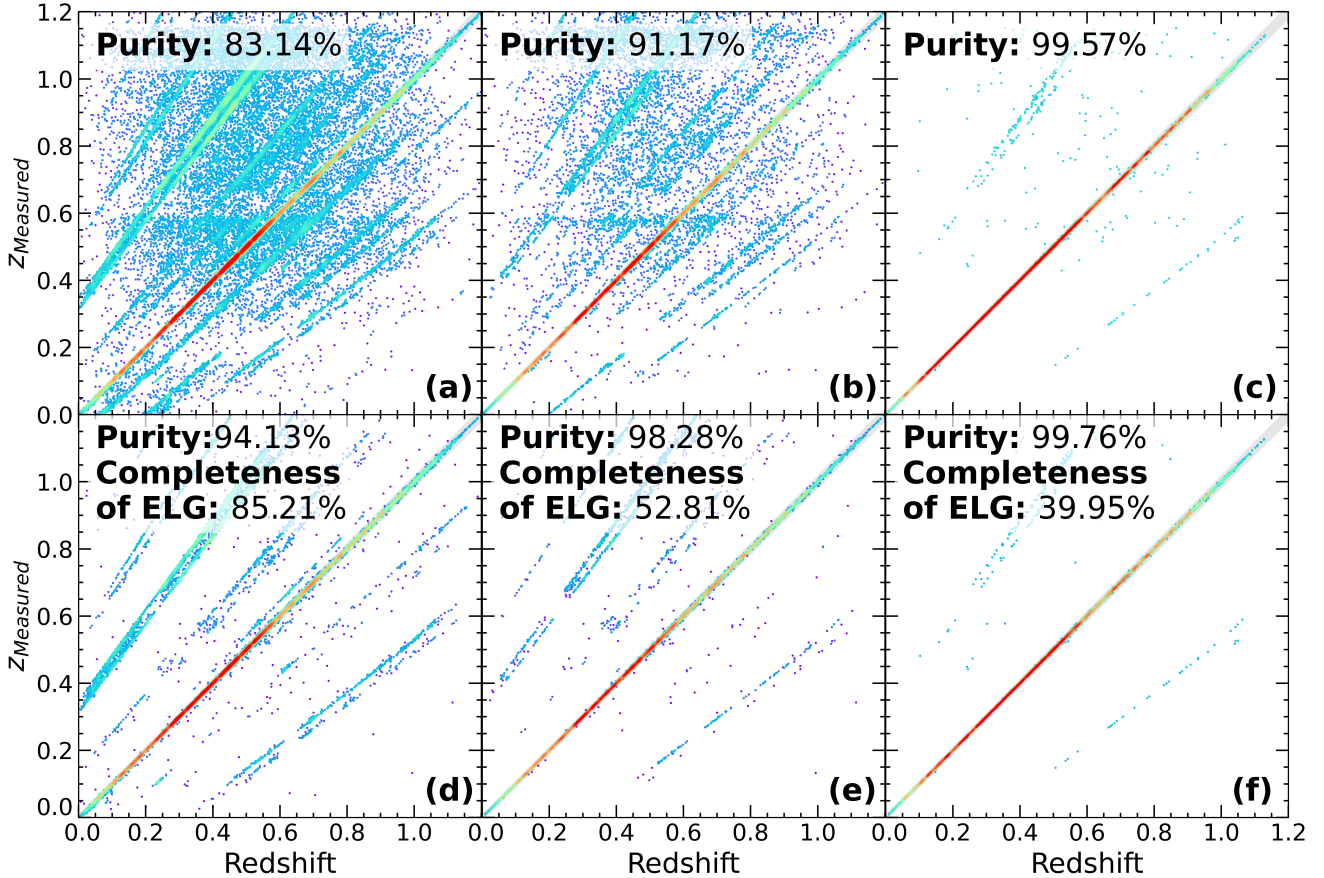


**Figure 11.** Comparisons of measured and true redshifts for various sample selections. The top panels correspond to measurable spectra, while the bottom panels pertain to ELGs. The left columns display comparisons for all samples. The middle columns focus on samples with ZWARNING = 0, and the right columns showcase samples with both ZWARNING = 0 and  $N_{\text{line}} \geq 3$ . The color indicates the number density, with red representing higher density.

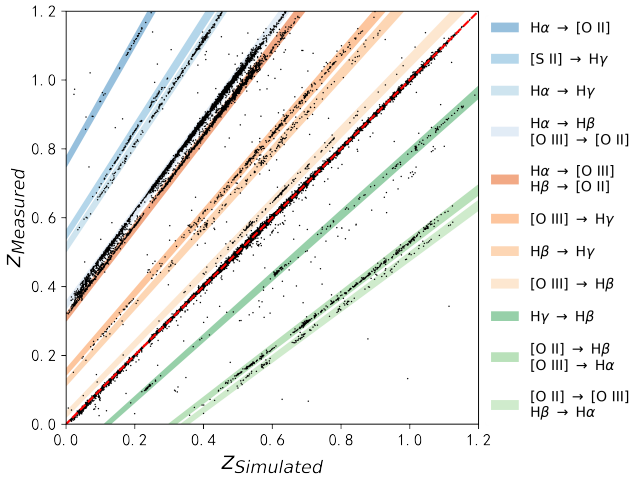


**Figure 12.** An example of emission line matching degeneracy of identified ELGs. The black dots in both figures correspond to the positions indicated in Fig. 11(d), without the use of colour to denote density. The red dashed diagonal indicates the location of the successful redshift measurement. The coloured strips are the possible ranges of failed measurements caused by emission confusion, with permissible error range  $|\Delta z_{\text{norm}}| < 0.01$ .

**Table 5.** Common Matching Confusion of Emission Lines

	Measurable ELGs		Measurable Spectra	
	All	ZWARNING = 0	All	ZWARNING = 0
No Confusion	94.13%	98.28%	83.14%	91.17%
$H\alpha \rightarrow H\beta$	2.34%	0.57%	3.44%	1.24%
$[O III] \rightarrow [O II]$	0.05%	0.00%	0.00%	0.00%
$H\alpha \rightarrow [O III]$	2.05%	0.44%	2.44%	0.73%
$H\beta \rightarrow [O II]$	0.25%	0.10%	0.33%	0.13%
$[O II] \rightarrow H\beta$	0.20%	0.12%	0.82%	0.46%
$[O III] \rightarrow H\beta$	0.20%	0.17%	0.70%	0.64%
$H\alpha \rightarrow H\gamma$	0.11%	0.01%	0.18%	0.04%
$H\gamma \rightarrow H\beta$	0.11%	0.01%	0.50%	0.12%
$H\beta \rightarrow H\gamma$	0.09%	0.06%	0.40%	0.26%
$H\alpha \rightarrow [O II]$	0.07%	0.11%	0.21%	0.30%
$[O II] \rightarrow [O III]$	0.06%	0.01%	0.10%	0.03%
$H\beta \rightarrow H\alpha$	0.06%	0.00%	0.27%	0.15%
others	0.34%	0.11%	7.46%	4.74%

all measurable spectra, along with the redshift covering rates for both sample groups. It reveals that including non-optimal redshift values in the analysis has led to enhancements in redshift measurement success rates. The redshift covering rates are notably high at 89 per cent

**Table 6.** Redshift success rates for different redshift outputs

	ELG	Measurable
First redshift output	85.21%	83.14%
Second redshift output	3.76%	4.50%
Third redshift output	0.19%	0.25%
Total covering rate	89.14%	87.89%

for ELGs and 88 per cent for all measurable galaxies. This indicates that even if the primary redshift estimate is inaccurate, reliable alternatives can be obtained from the secondary outputs. By incorporating additional information such as photometric redshift estimates or colors to constrain the redshift range and mitigate the degeneracies, we can achieve higher completeness and purity in our analyses. This also enables accurate redshift determinations for galaxies even with only one identifiable emission line.

## 6 SUMMARY

China is planning to launch the CSST with a large field of view in the near-Earth orbit. This telescope has both multi-wavelength imaging and slitless spectroscopic capabilities, enabling to conduct a sky survey covering an area of about 17,500 deg<sup>2</sup>. The survey will provide unprecedented data for exploring the Universe, especially the dark matter and energy. The high spatial resolution in comparative to HST will also make it beneficial for studying structure of galaxies in the near field and faraway. The CSST slitless spectroscopy is characterised by the wide wavelength coverage, same sky coverage as the multi-wavelength imaging, and deep limiting magnitude. The accurate redshift determination will be crucial for exploring the large-scale structure and galaxy formation in relatively low-redshift universe.

This paper describes the development and validation of a redshift measurement method relying on emission lines of galaxies, specifically designed for slitless spectra of the upcoming CSST. Key steps in determining a redshift using emission lines include identifying emission lines within the spectrum and matching them with their corresponding rest-frame wavelengths. Initially, potential emission lines are tentatively identified based on features like prominence, widths, and SNRs in the processed spectra. By comparing the peak wavelengths of these candidate emission lines with template emission-line wavelengths, a set of possible redshifts are derived. At each potential redshift, Gaussian fittings are employed to precisely determine the central wavelengths of emission lines, where those adjacent blended lines are fitted together. In addition, intrinsic flux ratio between different emission lines are applied to constrain the line matching and reduce the possible redshift degeneracy. Three top ranked redshift and corresponding quality flags are provided.

The redshift measurements are validated using a sample of slitless spectra simulated by CESS, as detailed in our previous work (Paper II). From the approximately one million spectra analysed, around 22 per cent of them are identified as ELGs. The purity of all measurable spectra stands at 83 per cent, while the completeness for ELGs reaches approximately 85 per cent. The study also investigates how SNR, redshift, and magnitude impact completeness, purity, and accuracy. These metrics indicate enhancements with higher SNR levels alongside decreasing redshifts. As the magnitude increases, the completeness and accuracy of ELG decrease, while the purity increases slightly. Redshift degeneracies arising from the confusion of various emission line combinations are thoroughly examined, with all potential confusions enumerated. To circumvent such confusions

effectively, restrictions on emission-line flux ratios are suggested. By integrating redshift quality indicators (ZWARNINGS) into the analysis, we find a notable reduction of degeneracies through stringent ZWARNING criteria. The study underscores the significance of multiple matched emission lines in enhancing completeness, purity, and the accuracy of redshift measurements. Notably, improved purity and completeness are achieved with a higher number of matched emission lines, accentuating the necessity of multiple emission line matches for robust redshift determinations. Additionally, we elucidate that even failed measurements may harbor the correct redshifts among secondary output values. However, in scenarios without ample prior information to constrain the redshift range and pinpoint the emission-line redshift, including cases with just a single emission line, supplementary constraints become crucial to effectively refine the redshift determination process.

The analyses presented in the study are founded solely on simulated spectra and assumptions regarding the instrument capabilities. To ensure the efficacy of emission-line redshift measurements using actual observational data from the forthcoming CSST, advancements in the configuration of the redshift measurement process are imperative.

## ACKNOWLEDGEMENTS

The authors acknowledge the supports from the National Key R&D Program of China (grant Nos. 2023YFA1607800, 2022YFA1602902, 2023YFA1607804, 2023YFA1608100, and 2023YFF0714800), and the National Natural Science Foundation of China (NSFC; grant Nos. 12120101003, 12373010, 12173051, and 12233008), and the Beijing Municipal Natural Science Foundation (grant No. 1222028). The authors also acknowledge the science research grants from the China Manned Space Project with Nos. CMS-CSST-2021-A02 and CMS-CSST-2021-A04 and the Strategic Priority Research Program of the Chinese Academy of Sciences with Grant Nos. XDB0550100 and XDB0550000.

## REFERENCES

- Aihara H., et al., 2018, *PASJ*, **70**, S4
- Albrecht A., et al., 2006, *arXiv e-prints*, pp astro-ph/0609591
- Bartelmann M., Schneider P., 2001, *Phys. Rep.*, **340**, 291
- Benitez N., et al., 2014, *arXiv e-prints*, p. arXiv:1403.5237
- Brammer G., 2023, grizli, Zenodo, doi:10.5281/zenodo.8210732
- Cao Y., et al., 2018, *MNRAS*, **480**, 2178
- Cervantes-Cota J. L., Smoot G., 2011, in Ureña-López L. A., Aurelio Morales-Técotl H., Linares-Romero R., Santos-Rodríguez E., Estrada-Jiménez S., eds, American Institute of Physics Conference Series Vol. 1396, VIII Workshop of the Gravitation and Mathematical Physics Division of the Mexican Physical Society. AIP, pp 28–52 (arXiv:1107.1789), doi:10.1063/1.3647524
- Colless M., et al., 2001, *MNRAS*, **328**, 1039
- DESI Collaboration et al., 2016, *arXiv e-prints*, p. arXiv:1611.00036
- Dark Energy Survey Collaboration et al., 2016, *MNRAS*, **460**, 1270
- Dey A., et al., 2019, *AJ*, **157**, 168
- Dressel L., Marinelli M., 2023, in, Vol. 15, WFC3 Instrument Handbook for Cycle 31 v. 15.0. p. 15
- Gong Y., et al., 2019, *ApJ*, **883**, 203
- Green J., et al., 2012, *arXiv e-prints*, p. arXiv:1208.4012
- Gu Y., et al., 2024, *MNRAS*, **529**, 4015
- Han Y., Han Z., 2019, *ApJS*, **240**, 3
- Kaiser N., 1987, *MNRAS*, **227**, 1
- Kewley L. J., Nicholls D. C., Sutherland R. S., 2019, *ARA&A*, **57**, 511
- LSST Science Collaboration et al., 2009, *arXiv e-prints*, p. arXiv:0912.0201

- Lan T.-W., et al., 2023, [ApJ](#), **943**, 68
- Laureijs R., et al., 2011, arXiv e-prints, p. arXiv:1110.3193
- Peebles P. J., Ratra B., 2003, *Reviews of Modern Physics*, **75**, 559
- Peebles P. J. E., Yu J. T., 1970, [ApJ](#), **162**, 815
- Penzias A. A., Wilson R. W., 1965, [ApJ](#), **142**, 419
- Planck Collaboration et al., 2020, [A&A](#), **641**, A6
- Riess A. G., et al., 1998, [AJ](#), **116**, 1009
- Tamura N., et al., 2016, in Evans C. J., Simard L., Takami H., eds, Society of Photo-Optical Instrumentation Engineers (SPIE) Conference Series Vol. 9908, Ground-based and Airborne Instrumentation for Astronomy VI. p. 99081M ([arXiv:1608.01075](#)), doi:10.1117/12.2232103
- Trimble V., 1987, [ARA&A](#), **25**, 425
- Wallisch B., 2019, *Review of Modern Cosmology*. Springer International Publishing, Cham, pp 9–47, doi:10.1007/978-3-030-31098-1\_2, [https://doi.org/10.1007/978-3-030-31098-1\\_2](https://doi.org/10.1007/978-3-030-31098-1_2)
- Wen R., et al., 2024, [MNRAS](#), **528**, 2770
- Woodfinden A., Percival W. J., Nadathur S., Winther H. A., Fraser T. S., Massara E., Paillas E., Radinović S., 2023, [MNRAS](#), **523**, 6360
- Wright E. L., et al., 2010, [AJ](#), **140**, 1868
- York D. G., et al., 2000, [AJ](#), **120**, 1579
- Zhan H., 2011, *Scientia Sinica Physica, Mechanica & Astronomica*, **41**, 1441
- Zhan H., 2021, *Chinese Science Bulletin*, **66**, 1290
- Zou H., et al., 2017, [PASP](#), **129**, 064101

This paper has been typeset from a Te<sub>X</sub>/L<sup>A</sup>T<sub>E</sub>X file prepared by the author.